A QUADRILATERAL VORTEX METHOD APPLIED TO CONFIGURATIONS WITH HIGH CIRCULATION

Brian Maskew
Analytical Methods, Inc.

SUMMARY

A quadrilateral vortex-lattice method is briefly described for calculating the potential flow aerodynamic characteristics of high-lift configurations. It incorporates an iterative scheme for calculating the deformation of force-free wakes, including wakes from side edges. The method is applicable to multiple lifting surfaces with part-span flaps deflected, and can include ground effect and wind-tunnel interference. Numerical results, presented for a number of high-lift configurations, demonstrate rapid convergence of the iterative technique. The results are in good agreement with available experimental data.

INTRODUCTION

The calculation of aerodynamic characteristics for three-dimensional configurations with high circulation, e.g., a wing with flap and tailplane can be misleading unless the trailing vortex wakes are represented correctly. In fact, initial applications of a quadrilateral vortex-lattice method with rigid non-planar wake (refs. 1 and 2) showed that results for a wing alone were sensitive to wake location at even moderate lift coefficients. The high circulation case, therefore, is non-linear, and requires a force-free wake representation.

The problem of calculating vortex sheet roll-up has recieved considerable attention in the past, (see review by Rossow (ref. 3)), but has been concerned mainly with the two-dimensional case. More recent work has included three-dimensional factors. Butter and Hancock (ref. 4) and also Hackett and Evans (ref. 5) included the influence of a bound vortex, and Belotserkovskii (ref. 6) incorporated a wake roll-up procedure with a vortex-lattice method. Mook and Maddox (ref. 7) developed a vortex-lattice method with leading-edge vortex roll-up. The roll-up procedure incorporated in the quadrilateral vortex method (ref. 2) differs slightly from the above methods, and is described here before discussing the high-lift applications.

10

SYMBOLS

α	incidence, in degrees
S	area
c	chord
$\bar{c}$	reference chord
A	aspect ratio
η	spanwise position normalised by wing semispan
C_L	lift coefficient
C_M	pitching moment coefficient (about the mid chord)
C_{D_i}	induced drag coefficient
k	induced drag factor, $= \pi A \, C_{D_i} / C_L^2$

Subscripts:

W	wing
T	tailplane or wind tunnel
calc	calculated
exp	experimental

METHOD DESCRIPTION

The method, which incorporates an iterative procedure for wake shape, is based on vortex-lattice theory (e.g., ref. 8), but the lattice is formed into quadrilateral vortices (fig. 1) instead of horse-shoe vortices. The quadrilateral form is equivalent to a piecewise constant doublet distribution and each vortex "panel" is self-contained. This makes it easier to apply to cambered surfaces. Another advantage is that only the quadrilaterals adjacent to trailing edges (and to side edges when edge separation is included) have trailing vortices, and so they are the only panels whose influence coefficients vary in the iterations for wake shape. The complete matrix of influence coefficients would be affected for the horse-shoe vortex model.

For the wake model, each trailing vortex is divided into straight segments (fig. 1), the number and length of which can be varied from vortex to vortex to allow more detailed representation in roll-up regions. The segmented part of each vortex ends in a semi-infinite vortex in the free-stream direction. In the iterative wake procedure, each trailing vortex segment is made approximately force-free by aligning it with the local mean velocity vector. The segment midpoint is the most appropriate position to apply this condition, yet most methods use the upstream end of the segment (following ref. 6). The present method calculates the mean velocity at 55% of the segment length (extrapolated from the previous segment) after examining a roll-up calculation (ref. 2) for a pair of equal strength, segmented vortices. Compared with the upstream end point, the 55% point gives faster convergence, and the results are less sensitive to segment length, (fig. 2).

Small Rankine vortex cores are placed on the vortices to avoid large velocities being calculated near the vortices; nevertheless, when calculating the velocity vectors for the wake relaxation, the local vortex contribution is excluded. To obtain the first vortex strength solution, the trailing vortices are assumed semi-infinite in the free-stream direction. A new vortex strength solution is obtained after each wake relaxation is completed.

RESULTS AND DISCUSSION

Wing-flap-tailplane

The wing-flap-tailplane configuration is a typical problem facing the aerodynamicist when calculating the behavior of an aircraft during landing and take-off. The present method enables the free-air and the ground-effect regimes to be evaluated. An illustrative calculation was performed for the part span flap configuration shown in figure 3(a). The geometric characteristics are presented in table 1.

Figure 3(a) shows the calculated vortex trajectories in free air after the fourth iteration. The vortex roll-up region from the flap edge passes close to the tailplane tip (outboard and below) and has clearly influenced the tailplane tip vortex trajectory (compare vortex (15) with vortex (10) from the wing tip, especially in the side view). The plan view shows wing inboard trailing vortices passing directly below the centers of tailplane quadrilaterals. If these vortices had been close to the tailplane surface, then the results would have diverged. In its present form, the method is not applicable to close approach problems unless the vortex trajectories are constrained to align with the local surface lattice. However, the close approach problem has been investigated, and a technique developed to overcome it (refs. 9 and 10) but, so far, this has not been incorporated in the main program.

The effect of iteration on the trajectory of vortex (7) from the flap edge region is given separately in figure 3(b). This vortex moved the most in the group; nevertheless, the figure shows little change between the third and fourth iterations. Sections through the calculated wakes in free air and in

ground effect are shown in figure 3(c). Compared with the free-air positions, the vortices move outwards in ground effect, and are deflected upwards. This movement will influence the ground-effect conditions at the tailplane.

Figure 4 shows the changes in wing and tailplane calculated lift and induced drag with iteration in free-air conditions. The wing lift is essentially converged by the second iteration and the induced drag factor, k, by the third. The tailplane lift and induced drag (in the presence of the wing) are essentially converged by the second iteration after a relatively big jump from the streamwise-wake value.

Table II gives the calculated values of lift and induced drag for free air and for ground-effect conditions, and includes values for wing and tailplane alone. These results imply (for the combined configuration) an average downwash angle at the tailplane of about 10.7° in free air and 1.7° in ground effect. The method, however, takes into account variations in downwash - and sidewash - across the span and chord of the tailplane. The presence of the tailplane causes small changes in the wing characteristics. In free air there is a small decrease in wing lift ($\approx 0.8\%$) and a small increase in induced drag factor (from 1.100 to 1.108), which result from a small downwash induced by the negative circulation on the tailplane. In ground effect, however, the tailplane - which now has positive lift - causes a small increase in wing lift and a decrease in its induced drag factor (from 0.613 to 0.581). Although the tailplane alone results show the expected increase in lift with ground effect, the wing-flap alone result shows a decrease. This apparent anomaly is in accordance with results found earlier in reference 11; with increasing camber and/or incidence, the initial increase in wing lift in ground effect decreases and eventually goes negative. This feature is made more apparent in the spanwise distribution.

The calculated spanwise load distribution, $C_L c/\bar{c}$, and center of pressure locus for the wing are shown in figures 5(a) and 5(b) for both free-air and ground-effect conditions. In ground effect (at the same incidence as in free-air) there is a relative loss in lift in the flapped region - evidently over the flap itself because the center of pressure moves forward there - while outboard there is a small increase in lift and a rearward shift in center of pressure (i.e., the normally accepted influences of ground effect). The net result, as already seen in table II, is a decrease in overall lift. Evidently, camber has a strong influence on the ground interference effect which must be taken into account when predicting aerodynamic characteristics near the ground (ref. 11).

As would be expected, the induced drag is concentrated over the flapped region in free air (fig. 5(c)), and in fact an induced thrust is calculated over the unflapped region - a plausible consequence of concentrating the load over the inboard part of a swept wing. In ground effect, the expected reduction in induced drag occurs mainly inboard of the flap edge region (i.e., in the upwash region from the flap edge trailing vortex image).

Wing-Flap in Wind Tunnel

Standard correction methods for wind-tunnel interference are largely based on image techniques, and assume the wing wake to be undeflected. When testing high-lift configurations, the trailing wake moves considerably from the basic wing plane, so unless the model is very small relative to the tunnel (with possible Reynolds Number problems), the real flow violates the assumptions. The present method calculates the wake shape in the presence of the model and the tunnel walls - the latter also being represented by a distribution of quadrilateral vortices. A calculation of this form would be particularly useful for wing-tailplane configurations, but sufficient elements were not available for a fair application to such a problem at this time (i.e., to cover wing, tailplane and wind tunnel). The results from a high-lift wing-flap calculation, therefore, are given here. The general arrangement is shown in figure 6, and the geometry is defined in table III. Lift values were available from unpublished wind-tunnel measurements on a blown-flap model.

Figure 7 shows the calculated vortex trajectories for $\alpha = 5^{\circ}$ in the wind tunnel. The lift coefficient is 2.14, and a correspondingly high rate of vortex roll-up is indicated. The tip vortex - which was allowed to separate from the flap hinge line to be more representative of the real flow conditions - moves steadily inboard as more vorticity is "entrained". The vortices just inboard of the tip have large "curvature" at the start, and ideally, should have had smaller segments there. A section through the calculated wake (fig. 7) is compared with that for free-stream conditions at approximately the same lift coefficient. This required a free-air incidence of 10° compared with 5° in the tunnel. In the tunnel, the roll-up region is squashed in a vertical sense and, on the whole, the vortex positions lie outboard relative to their positions in free air. In the tunnel, the vortices over the inboard region lie above the free-air position - a result of the reduced downwash in the tunnel.

Figure 8(a) shows the C_L characteristics calculated in the tunnel and in free air. The standard incidence correction (i.e., $\Delta\alpha = \delta C_L \, S_W/S_T$, with $\delta = 0.101$ here) applied to the in-tunnel values falls short of the free-air result by the order of 35%. Also shown are some values representing the experimental wind tunnel measurements with near critical blowing over the trailing-edge flap. These measurements were originally for a wing-body configuration, and have been modified to gross wing conditions. In view of this, they are included here only to indicate that the calculated in-tunnel $C_L \sim \alpha$ values are plausible. The modification for $C_{L_{gross}}$ applied to the measured net wing C_L was of the form:

$$\left(C_{L_{gross}} \right)_{exp} = \left(C_{L_{gross}} / C_{L_{net}} \right)_{theory} \left(C_{L_{net}} \right)_{exp}$$

The theoretical factor was obtained after applying the method first to the gross wing, and then to the net wing in the presence of a representative body. The factor was found to be a function of incidence, and varied from 1.145 at $\alpha = 0^{\circ}$ to 1.10 at $\alpha = 10^{\circ}$.

The calculated induced drag factor characteristics are shown in figure 8(b), and show a dependence on C_L in both free-air and in-tunnel conditions - the form of the dependence is not shown since only two points were calculated for each condition. The standard correction for drag ($\Delta C_{D_i} = C_L \times \Delta\alpha$) added to the calculated in-tunnel induced drag gave k values which fell short of the free-air calculations; the difference in the increment in k -

i.e., $(\Delta k_{calc} - \Delta k_{standard})/\Delta k_{calc}$

varied from 12% at $C_L = 1.98$ to 18% at $C_L = 2.14$.

Small Aspect Ratio Wing

For an extreme test case for the wake roll-up calculation, a slender rectangular wing of aspect ratio 0.25 was considered at 20° incidence. Calculations were performed using an 8 x 6 vortex array and two iterations for two configurations:

(a) flat plate

(b) bent plate (20° deflection about the mid chord)

Flow visualization studies and wind-tunnel force and moment measurements have been carried out on these configurations by Wickens (ref. 12). The real flow for these cases is dominated by the tip-edge vorticity, and surface viscous effects are relatively small; a comparison between the potential flow calculation and experiment is therefore practicable.

The side view and plan view of the calculated vortex trajectories from the flat and bent plates are presented in figures 9(a) and 9(b), respectively. Included in the side views are the approximate positions of the vortex cores from flow visualization (ref. 12) and the calculated centroid of vorticity locus. In the flat plate case, these lines are in excellent agreement, and in fact are inclined at approximately $\alpha/2$ to the surface - i.e., the theoretical angle for vanishingly small aspect ratio. In the bent plate case, two vortex cores appear in the experiment, one from the leading-edge tip and the other from the bend line tip - i.e., from the two peak vorticity regions. When calculating the centroid of vorticity locus for this case, the edge vortices were divided into two groups, the leading-edge vortex starting the first group, and the hinge-line vortex the second. The calculated centroid loci initially have fair agreement with the observed vortex cores, but later tend to diverge, indicating a slower rate of roll-up in the calculation. Another iteration might have helped here, but the proximity of the end of the segment-represented region (the extent of which was limited by the number of segments available in the program) must have influenced the shape near the downstream end.

Although the principal objective here was to observe the behavior of the vortex roll-up calculation under extreme conditions, it is interesting to see (fig. 10) that the calculated lift, drag and pitching moment are in reasonable agreement with the experimental measurements from reference 12; the flat plate results are particularly good, while the indications are that the bent plate calculations are not fully converged. In the latter case, the changes in the characteristics from the initial (streamwise) wake values to those from the second iteration are particularly large (see table IV).

Tip-Edge Separation

Earlier applications (unpublished) of the method to wings at large incidence (8 to 16°) gave poor correlation with experimental spanwise load distributions and wake deformation. The differences were attributable to the presence, in the experiment, of tip-edge vortices of the type calculated on the small aspect ratio wing. These effects are demonstrated here for a rectangular wing of aspect ratio 5.33 and at 12° incidence. The vortex lattice is shown in figure 11, and includes tip-edge vortices. The calculated vortex trajectories are shown after two iterations. Figure 12(a) shows the spanwise load distribution with and without the tip-edge vortices present. The edge separation gives a higher loading level towards the tip and a local bulge near the tip when using a large number of spanwise intervals. The bulge, consistently calculated using lattices with 15 and 25 spanwise intervals, is also apparent in the experimental load distribution from reference 13. (The lower lift level in the experiment is caused by an inboard separation resulting from the interaction between the wing and wall boundary layer.) The calculated lift coefficient increases from 0.85 to 0.93 with the tip-edge vortices.

The calculations indicate that the extra loading near the tip is carried on the rear of the wing; the center of pressure locus, (fig. 12(b)), shows a marked rearward movement near the tip with the tip-edge vortices compared with the usual forward movement calculated with the "linear" method. The locus is consistently calculated using 8, 15 and 25 spanwise intervals.

These edge effects, which are present also at flap edges, etc., have marked implications for calculations at high lift, affecting boundary layer development, tip vortex formation and trailing vortex sheet shape. However, further evaluation of these effects (such as detailed surface pressure distributions) would require the previously mentioned problem of close interference between discretized vortex sheets to be removed. For such applications, the method would need extending to include a near-field technique such as that developed in references 9 and 10.

CONCLUDING REMARKS

The quadrilateral vortex lattice method with the iterative wake relaxation procedure has been applied to a number of configurations with high circulation. The iterative procedure shows rapid convergence, and the calculations

are in good agreement with available experimental results. Tip-edge separation effects have been shown to be important aspects of high-lift calculations. More detailed theoretical evaluation of these effects, e.g., in terms of surface pressure distributions, would require extensions of the method to incorporate recently developed near-field techniques. Such an extension would also allow other close interference effects to be studied.

REFERENCES

1. Maskew, B.: Calculation of the Three-Dimensional Potential Flow Around Lifting Non-Planar Wings and Wing-Bodies Using a Surface Distribution of Quadrilateral Vortex Rings. TT7009, Loughborough Univ. of Technology, England, Sept. 1970.

2. Maskew, B.: Numerical Lifting Surface Methods for Calculating the Potential Flow about Wings and Wing-Bodies of Arbitrary Geometry. Ph.D. Thesis, Loughborough Univ. of Technology, England, Oct. 1972.

3. Rossow, V.J.: Survey of Computational Methods for Lift-Generated Wakes. NASA SP-347, March 1975, pp. 897-923.

4. Butter, D.J.; and Hancock, G.J.: A Numerical Method for Calculating the Trailing Vortex System Behind a Swept Wing at Low Speed. The Aeronautical Journal, Vol. 75, No. 728, Aug. 1971, pp. 564-568.

5. Hackett, J.E.; and Evans, M.R.: Vortex Wakes Behind High-Lift Wings. J. Aircraft, Vol. 8, No. 5, May 1971, pp. 334-340.

6. Belotserkovskii, S.M.: Calculation of the Flow Around Wings of Arbitrary Planform over a Wide Range of Angles of Attack. NASA TTF-12, 291, May, 1971.

7. Mook, D.T.; and Maddox, S.A.: Extension of a Vortex Lattice Method to Include the Effects of Leading-Edge Separation. J. Aircraft, Vol. 11, No. 2, Feb. 1974, pp. 127-128.

8. Rubbert, P.E.: Theoretical Characteristics of Arbitrary Wings by a Non-Planar Vortex Lattice Method. D6-9244, The Boeing Co., 1964.

9. Maskew, B.: A Subvortex Technique for the Close Approach to a Discretized Vortex Sheet. NASA TM X-62, 487, Sept. 1975.

10. Maskew, B.: A Submerged Singularity Method for Calculating Potential Flow Velocities at Arbitrary Near-Field Points. NASA TM X-73,115, March, 1976.

11. Maskew, B.: On the Influence of Camber and Non-Planar Wake on the Airfoil Characteristics in Ground Effect. TT7112, Loughborough Univ. Of Technology, England, Oct. 1971, (See also ARC 33950, 1973, Aero. Res. Council, London).

12. Wickens, R.H.: The Vortex Wake and Aerodynamic Load Distribution of Slender Rectangular Wings. Canadian Aeronautics and Space Journal, June 1967, pp. 247-260.

13. Chigier, N.A.; and Corsiglia, V.R.: Tip Vortices - Velocity Distributions. NASA TM X-62,087, 1971.

TABLE I. GEOMETRIC CHARACTERISTICS FOR THE WING-FLAP-TAILPLANE CONFIGURATIONS

General:	
Incidence	10°
Ground height (normalized by wing mean chord $\bar{c}$)	0.5
Wing:	
Aspect ratio	4
Sweep back	45°
Taper ratio	1
Flap chord/$\bar{c}$	0.25
Flap span/semispan	$0 \rightarrow 0.48$
Flap deflection: normal to hinge line	36°
in vertical streamwise plane	27°
Vortex quadrilateral array: across chord	3
across semispan	7
Tailplane:	
Aspect ratio	2
Sweep back	45°
Taper ratio	1
Span/wing span	0.4
(Distance aft from wing)/$\bar{c}$	2
(Distance above wing plane)/$\bar{c}$	0.2
Angle to wing plane	0°
Vortex quadrilateral array: across chord	3
across semispan	4

TABLE II. CALCULATED WING-FLAP-TAILPLANE LIFT AND INDUCED DRAG CHARACTERISTICS IN FREE AIR AND IN GROUND EFFECT (SECOND ITERATION)

Configuration		Wing-Flap		Tailplane (based on wing area)	
		C_L	k	C_{L_T}	$C_{D_{i_T}}$
Free-air	together	0.9613	1.108	-0.0104	-0.00206
	alone	0.9691	1.100	0.1279	0.00761
Ground-Effect	together	0.9388	0.581	0.1067	0.01119
	alone	0.9385	0.613	0.1441	0.00757

TABLE III. BASIC CHARACTERISTICS FOR THE WING-FLAP IN WIND-TUNNEL CONFIGURATION

Theoretical Model

Wing:

Aspect Ratio	2.9
Taper Ratio	0.55
Leading edge sweepback	31^{o}
Trailing-edge flap:	
Span/wing span	1.0
Chord/wing chord	0.31
Deflection (normal to hinge line)	40^{o}
Hinge-line sweepback	17^{o}
Vortex quadrilateral array (chordwise x spanwise)	3 x 10

Wind Tunnel:

Wing span/tunnel width	0.56
Wing area/tunnel cross section area (S_W/S_T)	0.256
Tunnel 'length'/wing mean chord	6
Vortex quadrilateral array (lengthwise x circumferential)	11 x 10

Experiment

Reynolds Number (based on wing mean chord)	1.2×10^{6}

Gross Wing:

Basic details are the same as for theoretical model, but in addition:

Leading edge flap:	
Full net span	
Chord/wing chord	0.15
Deflection	40^{o}
Hinge-line sweepback	28^{o}
Trailing-edge flap blowing momentum coefficient (critical value at $\alpha = 8^{o}$)	0.018

Body:

Width	0.18*
Depth	0.36*
Length	1.834*
Length of fore and aft fairings	0.357*+
Wing position (above body center line)	0.096*
Section - rectangular with rounded corners	

* Note: normalised by gross wing semispan + (each)

TABLE IV. CALCULATED CHARACTERISTICS FOR SLENDER RECTANGULAR WINGS (ASPECT RATIO = 0.25)

Configuration	Wake	C_L	C_{D_i}	C_M (½ chord)
Flat Plate $\alpha = 20^0$	Streamwise	0.7489	0.2633	0.1069
	First Iteration	0.5301	0.1725	0.1111
	Second Iteration	0.5301	0.1654	0.1116
Bent Plate $\alpha = 20^\circ$ Bend = 20°	Streamwise	1.9508	1.5405	-0.056
	First Iteration	1.0934	0.6174	0.078
	Second Iteration	1.1241	0.6381	0.075

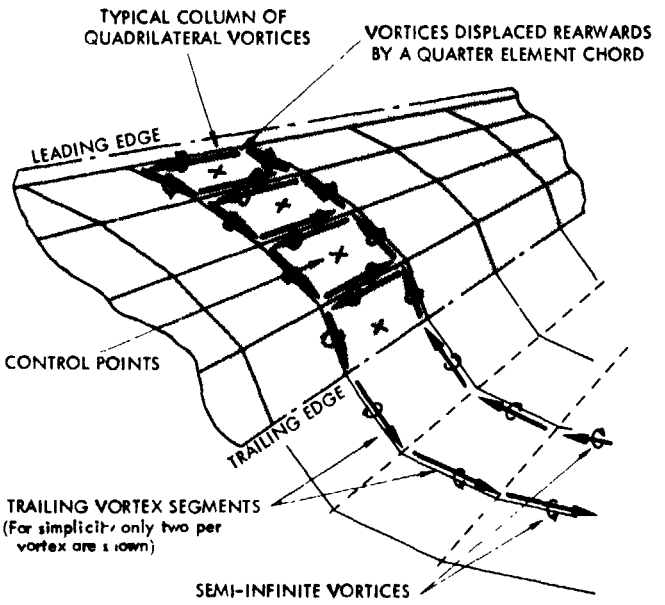

Figure 1.- Quadrilateral vortex model.

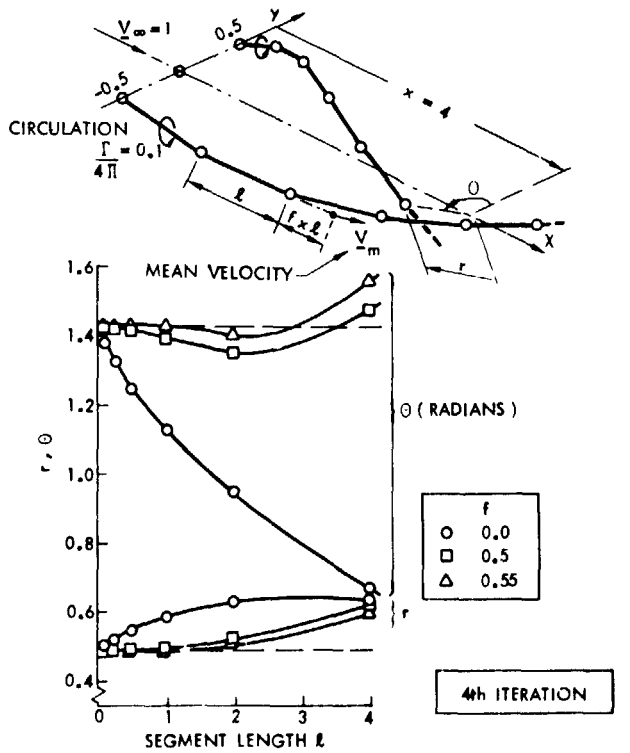

Figure 2.- Calculated roll-up of a pair of segmented vortices.

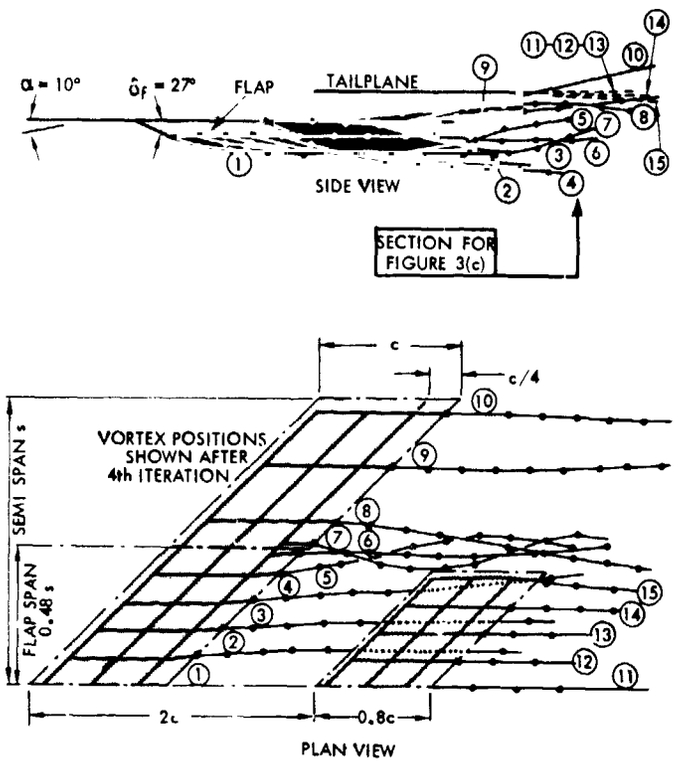

(a) Configuration and general views after four iterations.

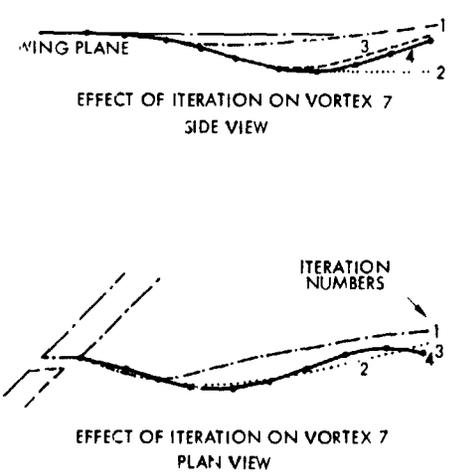

(b) Effect of iteration on vortex (7) trajectory.

Figure 3.- Calculated vortex trajectories for a wing-flap-tailplane configuration in free air.

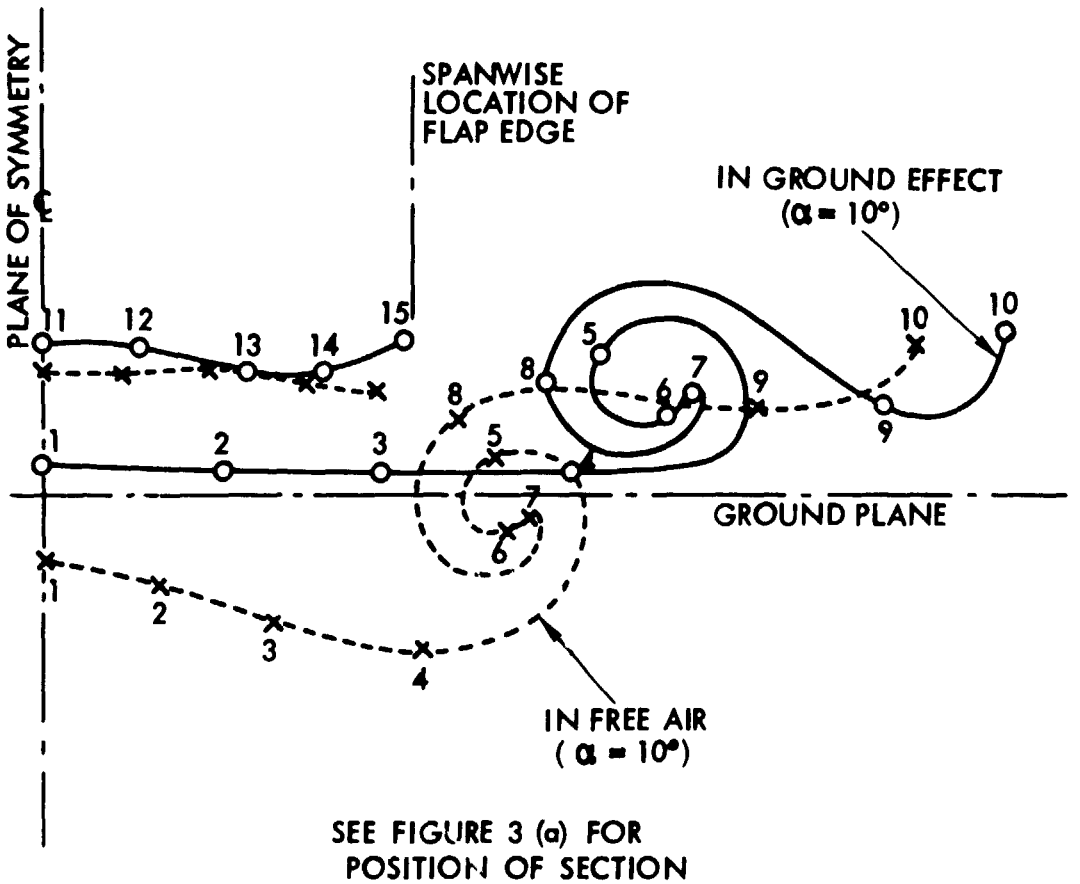

(c) Sections through the calculated wakes in free air and in ground effect.

Figure 3.- Concluded.

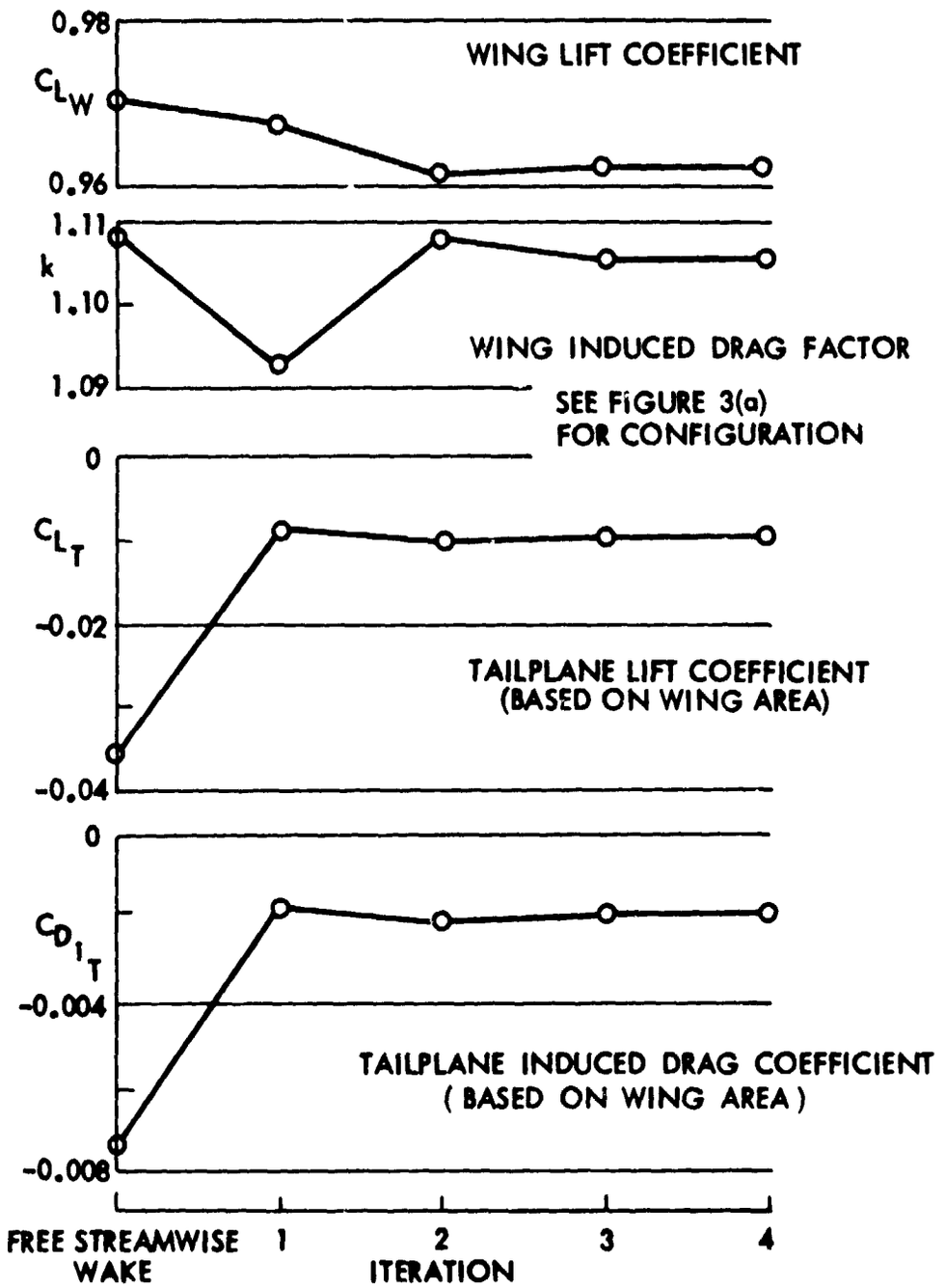

Figure 4.- Effect of iteration on the calculated lift and induced drag of the wing-flap-tailpiece configuration in free air.

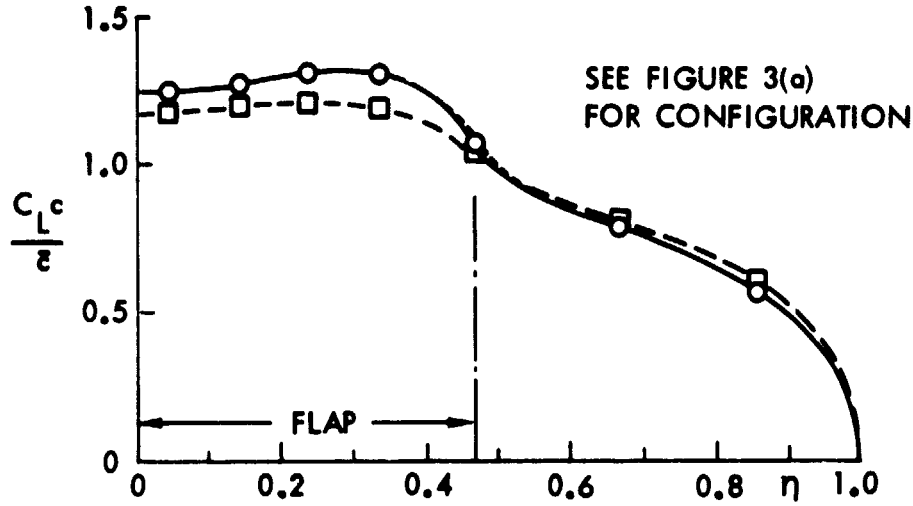

(a) Spanwise loading.

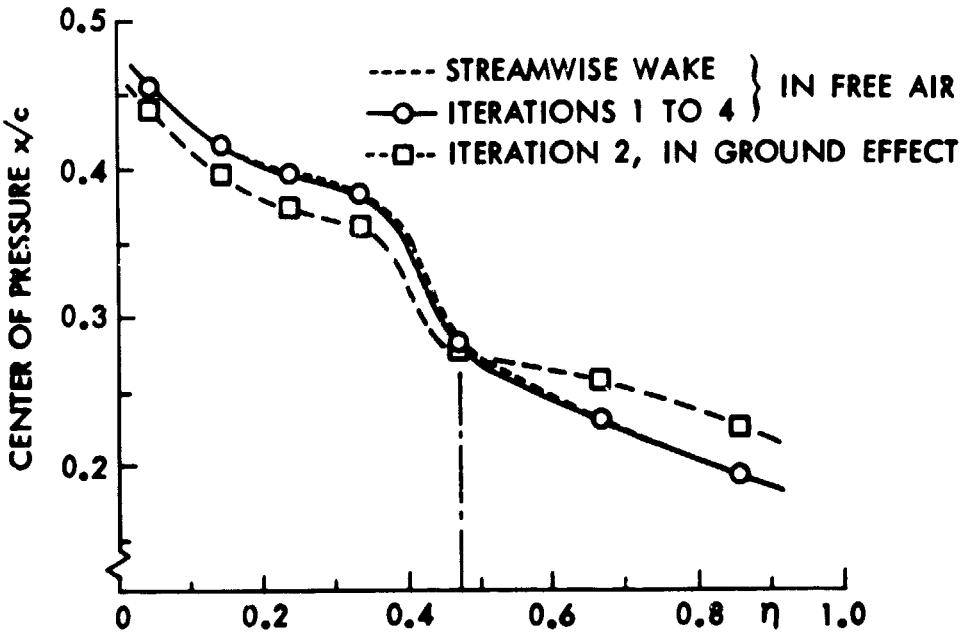

(b) Center of pressure locus.

Figure 5.- Calculated aerodynamic characteristics for the wing and inboard flap in the wing-flap-tailplane configuration in free air and in ground effect.

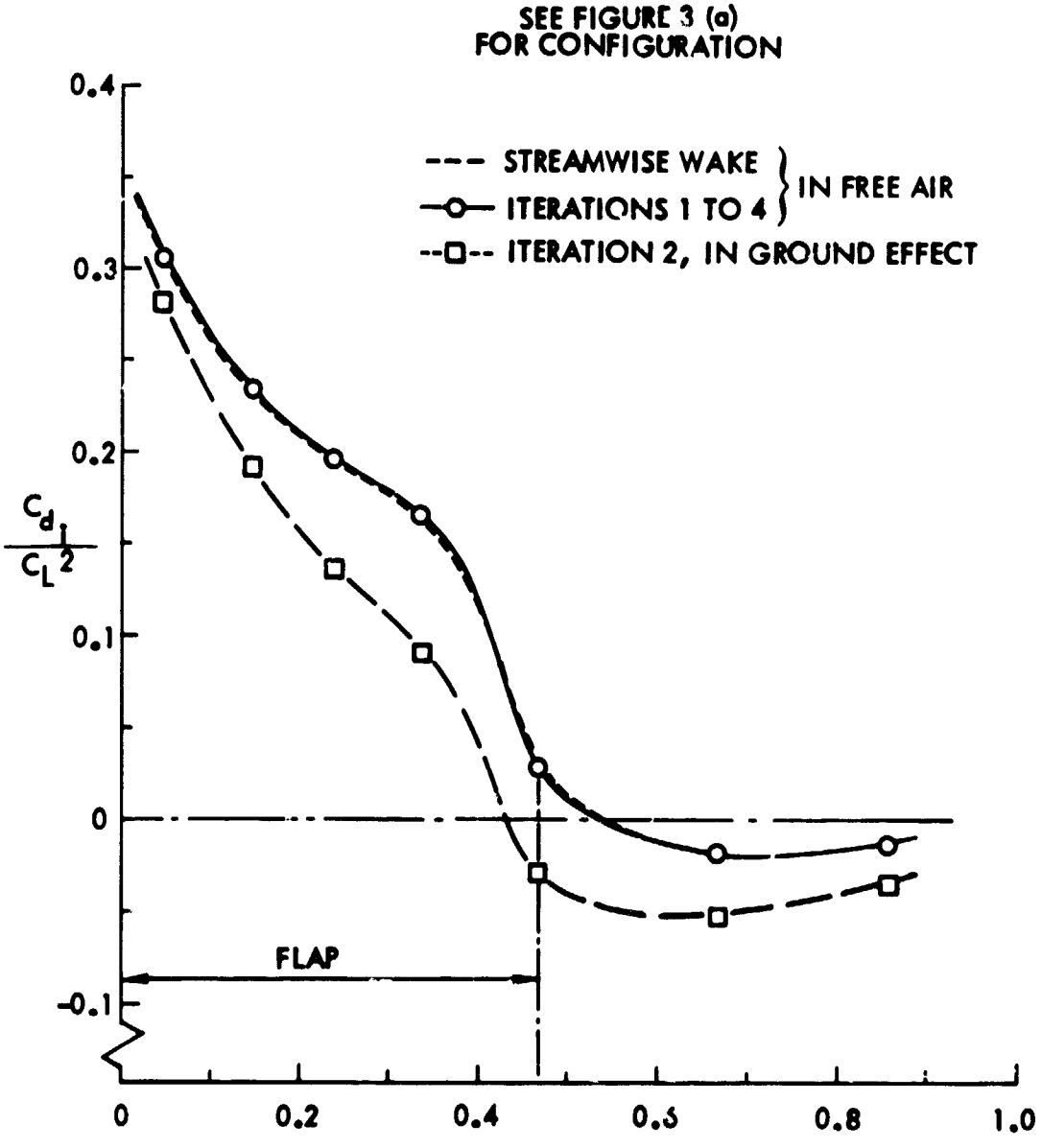

(c) Induced drag distribution.

Figure 5.- Concluded.

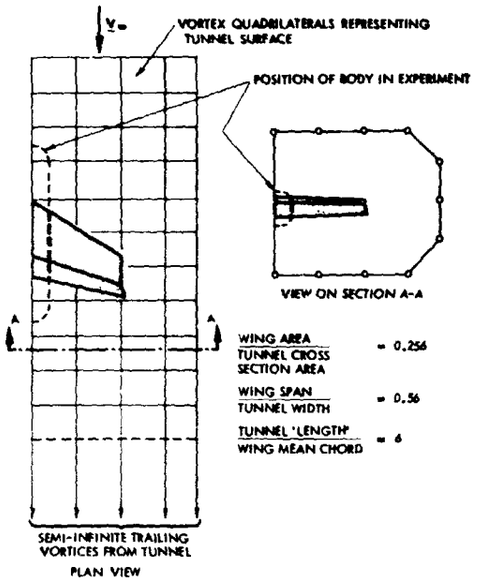

Figure 6.- Wing flap in wind tunnel - general arrangement of the theoretical model.

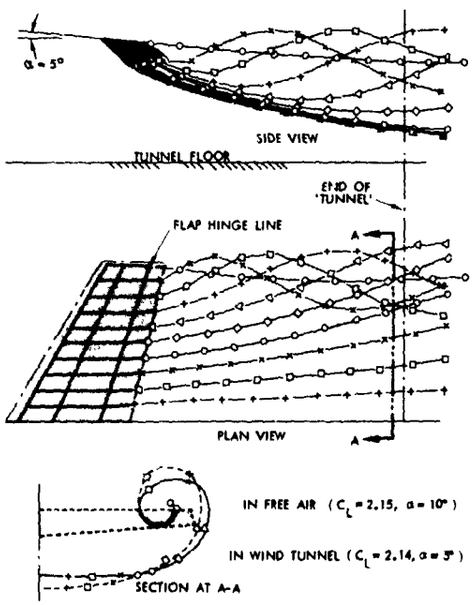

Figure 7.- Calculated vortex trajectories in wind tunnel.

C3

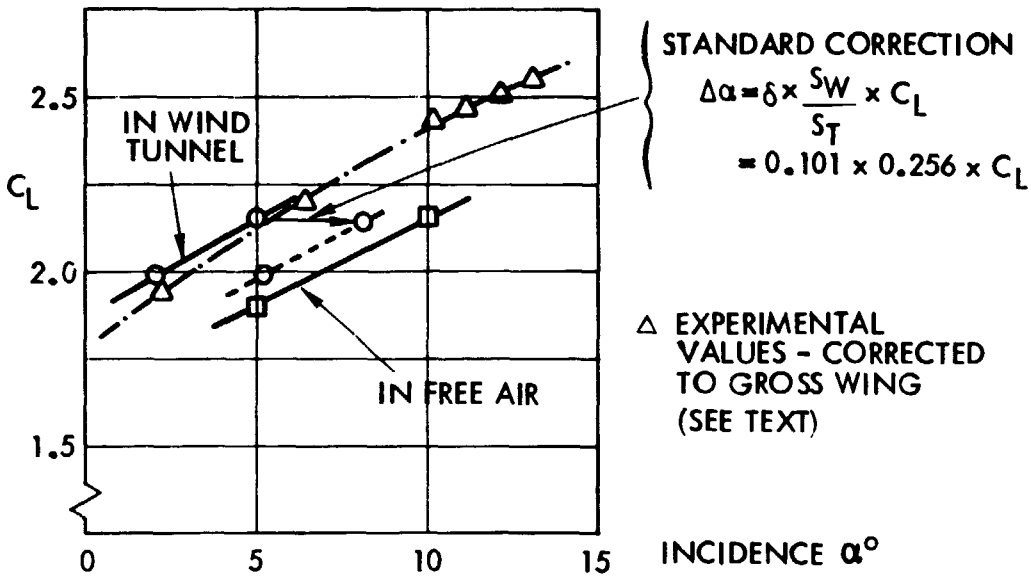

(a) Lift coefficient.

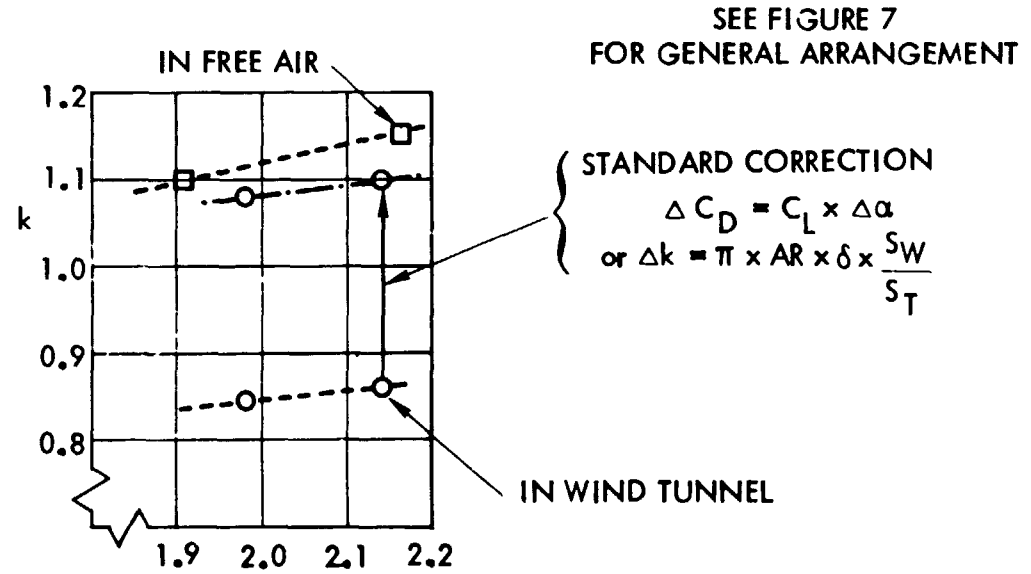

(b) Induced drag factor.

Figure 8.- Calculated aerodynamic characteristics of the wing-flap configuration in free air and in wind tunnel.

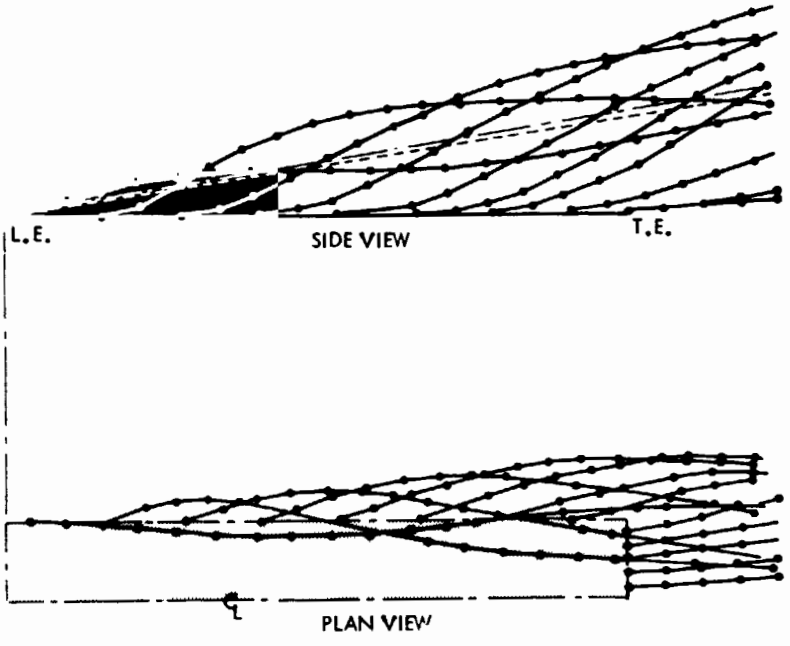

(a) Flat plate.

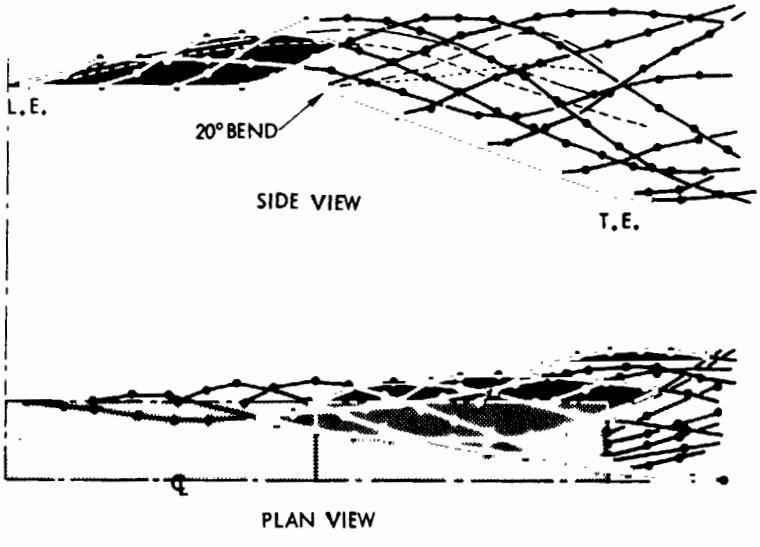

(b) Plate with 20^{o} mid chord bend.

Figure 9.- Calculated vortex trajectories for aspect ratio 0.25 wings at 20^{o} incidence.

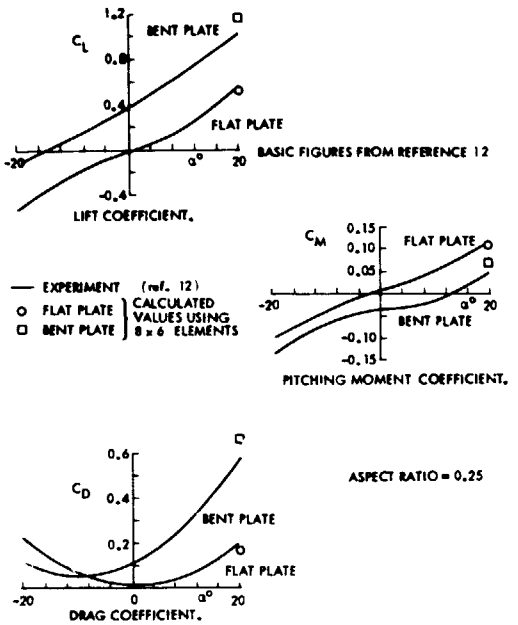

Figure 10.- Calculated aerodynamic characteristics for the small aspect ratio wings compared with experimental measurements.

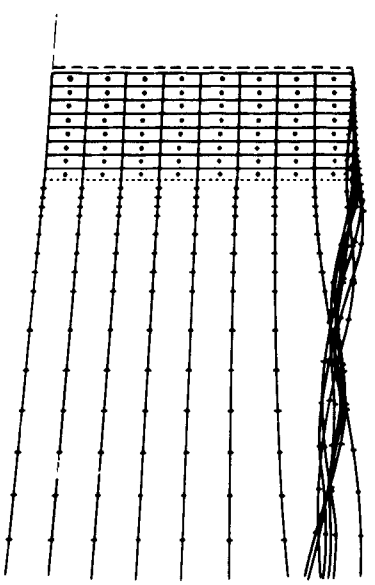

Figure 11.- Calculated vortex trajectories for an aspect ratio 5.33 rectangular wing at 12^{o} incidence after two iterations.

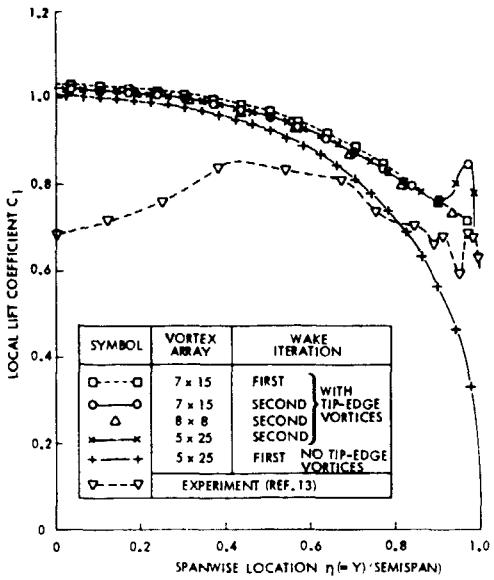

(a) Lift distribution.

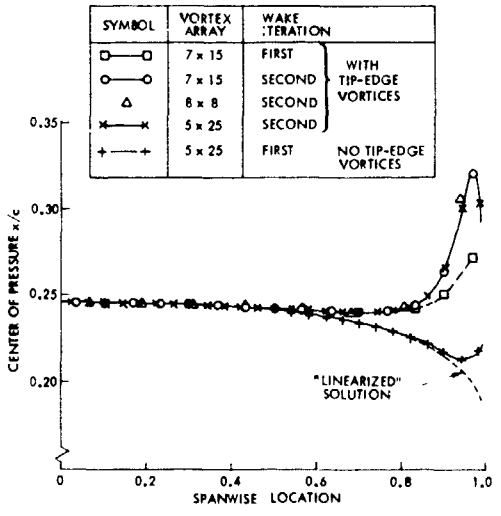

(b) Center of pressure locus.

Figure 12.- Calculated aerodynamic characteristics for the rectangular wing with and without tip edge vortices.